catalysts

MDPI

Article

CO_2 and H_2O Coadsorption and Reaction on the Low-Index Surfaces of Tantalum Nitride: A First-Principles DFT-D3 Investigation

Nelson Y. Dzade

School of Chemistry, Cardiff University, Main Building, Park Place, Cardiff CF10 3AT, UK; DzadeNY@cardiff.ac.uk

Received: 21 September 2020; Accepted: 16 October 2020; Published: 20 October 2020

Abstract: A comprehensive mechanistic insight into the photocatalytic reduction of CO_2 by H_2O is indispensable for the development of highly efficient and robust photocatalysts for artificial photosynthesis. This work presents first-principles mechanistic insights into the adsorption and activation of CO_2 in the absence and presence of H_2O on the (001), (010), and (110) surfaces of tantalum nitride (Ta_3N_5), a photocatalysts of significant technological interest. The stability of the different Ta_3N surfaces is shown to dictate the strength of adsorption and the extent of activation of CO_2 and H_2O species, which bind strongest to the least stable Ta_3N_5(001) surface and weakest to the most stable Ta_3N_5(110) surface. The adsorption of the CO_2 on the Ta_3N_5(001), (010), and (110) surfaces is demonstrated to be characterized by charge transfer from surface species to the CO_2 molecule, resulting in its activation (i.e., forming negatively charged bent $CO_2^{-\delta}$ species, with elongated C–O bonds confirmed via vibrational frequency analyses). Compared to direct CO_2 dissociation, H_2O dissociates spontaneously on the Ta_3N_5 surfaces, providing the necessary hydrogen source for CO_2 reduction reactions. The coadsorption reactions of CO_2 and H_2O are demonstrated to exhibit the strongest attractive interactions on the (010) surface, giving rise to proton transfer to the CO_2 molecule, which causes its spontaneous dissociation to form CO and $2OH^-$ species. These results demonstrate that Ta_3N_5, a narrow bandgap photocatalyst able to absorb visible light, can efficiently activate the CO_2 molecule and photocatalytically reduce it with water to produce value-added fuels.

Keywords: tantalum nitride (Ta_3N_5); photocatalysis; CO_2 activation; density functional theory (DFT)

1. Introduction

Photocatalytic reduction of carbon dioxide (CO_2) with water (H_2O) to produce value-added fuels such as such as CO, HCOOH, CH_3OH, and CH_4 is a promising route to reduce CO_2 emissions and address the global energy crisis [1–5]. The activation and reduction of CO_2 is, however, an energetically demanding process that involves multiple electron transfer reactions [6–10], hence highly efficient and robust photocatalysts are critical. Several photocatalysts, such as TiO_2 [11–13], In_2O_3 [14,15], Ga_2O_3 [16,17], Al_2O_3 [18,19], ZnO [20,21], CeO_2 [22,23], $ZnGe_2O_4$ [24], and $BiVO_4$ [25,26], have been investigated for their performance in catalysing CO_2 reduction. However, because of their large bandgaps and high charge-carrier recombination rates, most of these semiconductor materials have low CO_2 conversion efficiencies. Therefore, there is continuous active research to find novel photocatalytic materials that are active under visible/solar light.

Recently, many active visible light absorbers with narrow bandgaps, in particular Ta-based materials, such as tantalum nitrides (Ta_3N_5) and tantalum oxynitrides (TaON), have attracted a lot of attention owing to their unique catalytic properties [27]. Various forms of nanostructured Ta_3N_5

including nanorod, nanoparticle, hollow sphere, and thin films have been considered as photocatalysts with reported enhanced photocatalytic activities [28–32]. Ta_3N_5 and TaON have narrow band gap energies of 2.1 and 2.4 eV, respectively, which make them suitable to absorb visible light to initiate photocatalysis [33]. Due to its narrow bandgap energy, Ta_3N_5 could generate a sufficient number of electrons and holes even under visible light, which could directly reduce CO_2 into a radical anion ($CO_2^{-\delta}$) and reduce H_2O to protons (H^+). Several studies have been conducted on the application of Ta_3N_5 for water splitting and photocatalytic degradation of organic pollutants [15,16,34,35]. The obtained results indicated that the T_3N_5 is a promising candidate as a visible light-driven photocatalysis. Recently, the photocatalytic reduction of CO_2 to CO over Ta_3N_5 has been reported [36,37]. However, detailed mechanistic understanding of the interaction between CO_2 and Ta_3N_5 photocatalyst is still limited.

The adsorption and activation of CO_2 are the foremost and fundamental steps in the photocatalytic reduction of CO_2 on the surface of a photocatalyst [38–41]. Compared to the linear gas-phase molecule, chemisorbed CO_2 (mainly carbonate or $CO_2^{-\delta}$ anion) is characterized by a bent geometry with a decreased lowest unoccupied molecular orbital (LUMO), which favours charge transfer from the photoexcited semiconductors to the surface-adsorbed CO_2 molecules [41]. Generally, exposed surfaces with a smaller work function provide greater activation for CO_2 as they favour electron transfers [42]. In this work, a comparative first-principles density functional theory (DFT) study of the adsorption and activation of CO_2 in the absence and presence of H_2O on Ta_3N_5(001), (010), and (110) surfaces is presented. First, the structures and relative stabilities of the low-index (001), (010), and (110) surfaces were systematically characterized and the equilibrium crystal morphology of the Ta_3N_5 crystal was constructed based on calculated surface energies. Secondly, the fundamental adsorption and coadsorption geometries of CO_2 and H_2O, including the energetics and electronic properties are discussed. The stabilities of the coadsorbed CO_2–H_2O species on the various surfaces were also evaluated to determine the pathways for the surface reactions involving these species, and to characterize the stability of the different reduced forms of CO_2, in particular the formate and bicarbonate species that were identified experimentally [37].

2. Results and Discussion

2.1. Bulk and Surface Properties

Ta_3N_5 crystalizes in the orthorhombic structure, as shown in Figure 1a,b, with space group *Cmcm* (No. 63). The neutron diffraction-derived lattice parameters are a = 3.886 Å, b = 10.212 Å, c = 10.262 Å, and $\alpha = \beta = \gamma = 90°$ [43]. The structure of Ta_3N_5 is composed of octahedra of N atoms centred by Ta atoms. Since the N atoms are both three and four coordinated, the octahedra are irregular. The conventional unit cell consists of 32 atoms, where each Ta atom is bonded to six N atoms, while N atoms are bonded to three or four Ta atoms. The Ta–N distances in Ta_3N_5 range from 1.96 to 2.24 Å. From full relaxation (ions + cell shape + volume) until the required accuracy was reached, the lattice parameters of Ta_3N_5 were predicted at a = 3.921 Å, b = 10.317 Å, and c = 10.323 Å, in close agreement with experimental data [43] and earlier theoretical predictions [44–47]. The Ta–N distances for the N atoms coordinated to three Ta atoms were calculated at 2.000, 2.083, and 2.048 Å, whereas those for the N atoms coordinated to four Ta atoms are 2.117(×2) and 2.241(×2) Å. Figure 1c shows the partial density of states of Ta_3N_5, from which the band gap is estimated at 2.11 eV, which is in good agreement with ultraviolet–visible (UV–vis) spectroscopy measurements of Ta_3N_5 powders and thin films which estimate an optical gap of approximately 2.1 eV [48,49]. Previous theoretical studies based on GGA+U [45] and HSE06 [50,51] functionals predicted the bandgap in the range of 2.1–2.21 eV. It is evident from Figure 1c that the top of the valence band is mainly composed of N-2*p* orbitals, while the bottom of the conduction band is mainly composed of Ta-5*d* orbitals, indicating that transitions near the absorption edge occur between N-2*p* and Ta-5*d* orbitals, which is in agreement with earlier theoretical works [45,50,51].

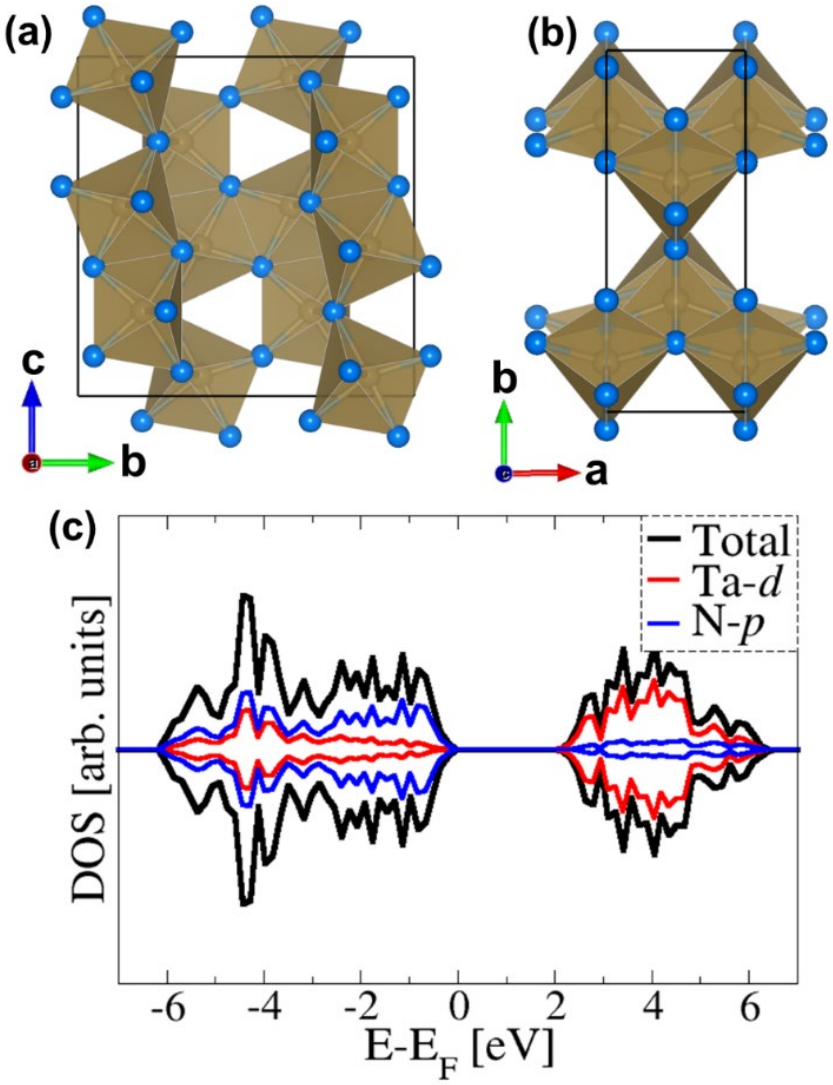

Figure 1. The orthorhombic crystal structure of Ta_3N_5 in terms of TaN_6 octahedra viewed in the (**a**) c–b and (**b**) b–a planes. (**c**) The electronic density of state of Ta_3N_5 showing the total and projection on the Ta *d* states and N *p* states. (Colour scheme: Ta = pale olive and N = blue.)

Figure 2 shows the optimized structures of the most stable terminations of the Ta_3N_5(001), (010), and (110) surfaces, which have calculated surface energies of 2.33, 2.04, and 1.58, Jm^{-2}, respectively. All surfaces are terminated by N atoms and exhibit step-like surface topologies. Using the calculated surfaces energies, the equilibrium Wulff shape of Ta_3N_5 nanocrystal was constructed, as shown in Figure 3. The Ta_3N_5 nanocrystal is found to exhibit an elongated shaped, with the (110) and (010) facets expressed in the rectangular crystal edges and the (001) facet enclosing the hexagonal edge. The predicted morphology is consistent with the elongated polyhedral crystal shape observed in experiments [30,52]. The differences in the structure, composition and stabilities of the (001), (010), and (110) surfaces are expected to dictate their reactivity towards CO_2 and H_2O molecules, which is investigated in detail and discussed in the following sections.

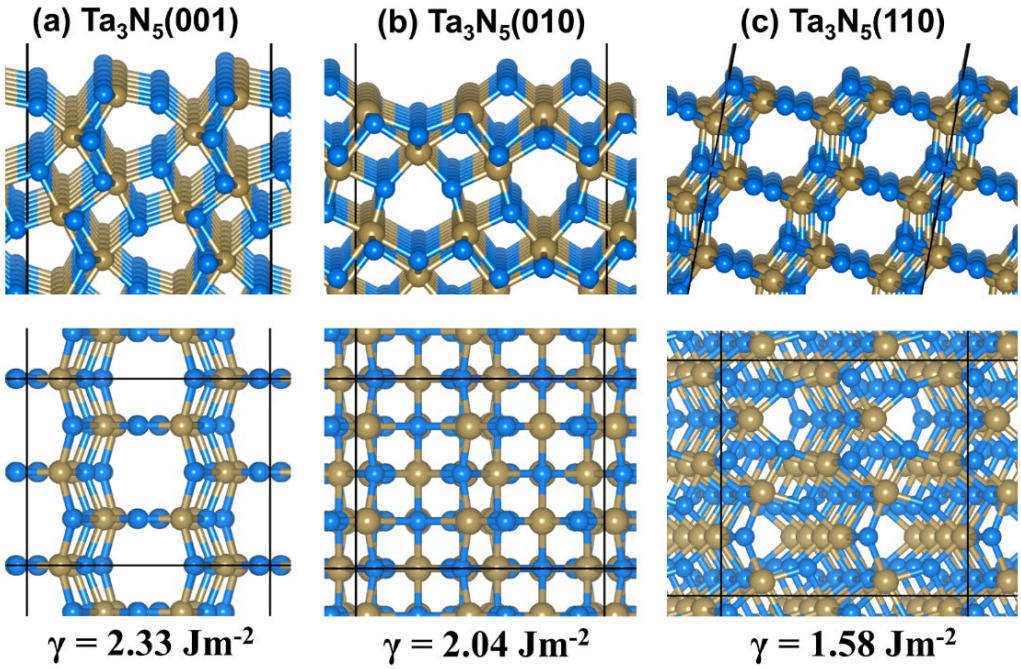

Figure 2. Optimized structures of the (**a**) {001}−(2 × 1), (**b**) {010}−(2 × 1), and (**c**) {110}−(1 × 1) surfaces of Ta_3N_5, in top (top) and side (bottom) views. (Atomic colour scheme: Ta = pale olive and N = blue.)

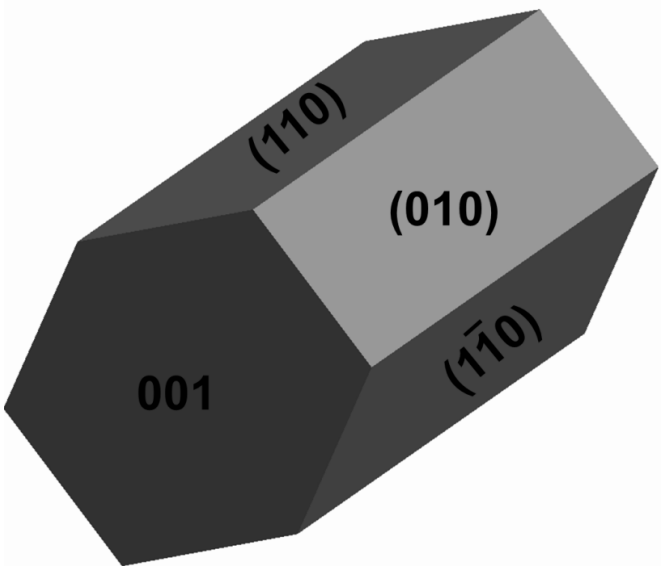

Figure 3. Equilibrium morphology of Ta_3N_5 nanocrystal derived from Wulff construction.

2.2. CO_2 Adsorption on (001), (010), and (110) Ta_3N_5 Surfaces

Considering that the initial step for CO_2 reduction is its activation [53], the lowest-energy adsorption configurations of CO_2 on the Low-Miller index (001), (010), and (110) Ta_3N_5 surfaces were first investigated in order characterize the strength of interaction and the extent of the C−O bond activation. Shown in Figure 4 are the lowest-energy adsorption geometries of CO_2 on the different Ta_3N_5(001), (010), and (110) surfaces, with the calculated adsorption energy and structural parameters summarized in Table 1. The less stable CO_2 adsorption geometries predicted on the different Ta_3N_5 surface are displayed in Supplementary Information Figures S1–S3. At the (001) surface, the CO_2 molecule interacts through all three atoms, as shown in Figure 4a, with the C atom bound to N sites

and the O atoms bound to Ta sites, releasing an adsorption energy of −2.73 eV. The interacting Ta−O and the N−C bonds were calculated at 2.176 and 1.361 Å, respectively. The strong adsorption induced structural transformation in the CO_2 molecules with the C−O bonds elongated from 1.176 Å in the gas phase to 1.301 Å in the adsorbed state and the $\angle O_aCO_b$ angle reduced to 130.0°, indicating activation of the CO_2 molecule. Compared to the (001), the CO_2 molecule interacts with the (010) surface via the carbon and one oxygen atom, as shown in Figure 4b, releasing an adsorption energy of −1.89 eV. The C−O bonds are significantly elongated, in particular the surface-bound one (1.422 Å) compared to the unbound one (1.202 Å) and the $\angle O_aCO_b$ angle is reduced to 123.9°. Similar to the (001) surface, CO_2 adsorption on the (110) surface involves all three atoms, as shown in Figure 4c, with the C atom binding at the N site and the O atoms bound to Ta sites, releasing an adsorption energy of −1.20 eV. Consistent with the weaker adsorption, longer Ta−O and the N−C bonds than on the (001) were calculated at 2.217 and 1.400 Å, respectively. The average C−O bond and $\angle O_aCO_b$ angle are calculated at 1.292 Å and 125.5°, respectively.

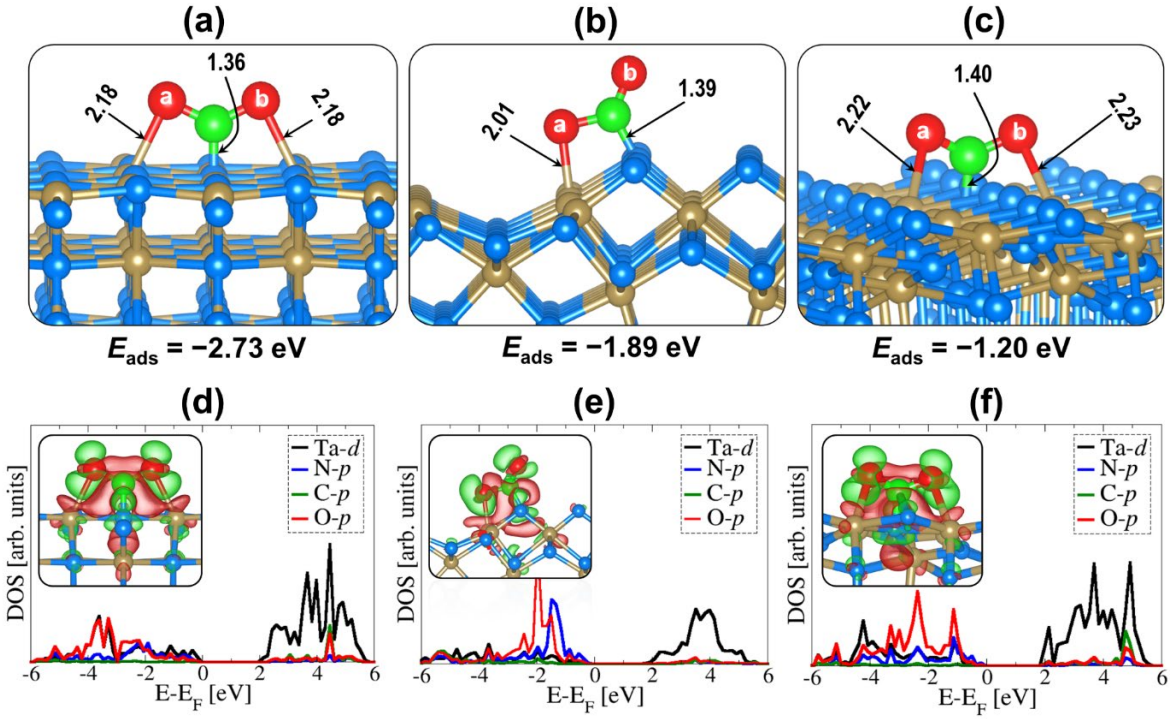

Figure 4. Lowest-energy CO_2 adsorption structures on (**a**) (001), (**b**) (010), and (**c**) (110) Ta_3N_5 surfaces. The DOS projected on the surface Ta *d* states and N *p* states interacting with the C and O *p* states of CO_2 (**d**–**f**) and the corresponding isosurface contours of the differential charge density are shown as inserts in (**d**–**f**), where green contours denote electron density increase and the red contours denote electron density decrease by 0.02 e/Å^3, respectively. (Atomic colour scheme: Ta = pale olive, N = blue, C = green, and O = red.)

Partial density of states (PDOS) and differential charge density isosurface contours analyses provided further atomic-level insights into the mixing atomic orbitals and redistribution of electron density within the CO_2-Ta_3N_5 systems. The adsorption of CO_2 on Ta_3N_5 surface is characterized by a strong mixing of interacting surface (Ta-*d* and N-*p*) and CO_2 (C-*p* and O-*p*) orbitals, as shown in Figure 4d–f. Consistent with chemisorption, electron density redistributions within the CO_2-Ta_3N_5 systems is observed, which was analysed through differential charge density isosurface contours, obtained as:

$$\Delta\rho = \rho_{CO_2+surface} - (\rho_{surface} + \rho_{CO_2}) \quad (1)$$

where $\rho_{CO_2+surface}$, $\rho_{surface}$ and ρ_{CO_2} are the electron density of the total CO_2-Ta_3N_5 system, the bare Ta_3N_5 surface, and the isolated CO_2 molecule as in the relaxed adsorbed configuration. The differential charge density iso-surface contours inserts in Figure 4d–f reveal a charge transfer from the bound surface ions into the π-antibonding orbital of the CO_2 molecule via the newly formed Ta−O and the N−C bonds. The CO_2 molecule gained a net charge of 0.40, 0.35 and 0.28 from the (001), (010), and (110) surfaces, resulting in the formation of negatively charged bent species ($CO_2^{\delta-}$) with elongated C−O bonds, confirmed by vibrational frequencies analyses, as shown in Table 1.

Table 1. Adsorption energies, geometrical parameters, charges, and vibrational frequencies of molecular CO_2 on Ta_3N_5(001), (010), and (110) surfaces.

Parameter	Free CO_2	Ta_3N_5(001)	Ta_3N_5(010)	Ta_3N_5(110)
E_{ads} (eV)	-	−2.73	−1.89	−1.20
$\Delta q(CO_2)$ (|e|)	0.0	0.40	0.34	0.31
d(C−O_a) (Å)	1.176	1.302	1.422	1.293
d(C−O_b) (Å)	1.176	1.301	1.202	1.290
∠O_aCO_b (°)	180.0	130.0	123.9	125.5
d(C−N) (Å)	-	1.361	1.396	1.400
d(O_a−Ta) (Å)	-	2.176	2.012	2.217
d(O_b−Ta) (Å)	-	2.180	-	2.230
υ_{as} (cm^{-1})	2373	1465	1804	1718
υ_s (cm^{-1})	1323	1265	911	881
υ_b (cm^{-1})	631	819	737	691

2.3. CO_2 Dissociation on (001), (010), and (110) Ta_3N_5 Surfaces

Shown in Figure 5 are the most stable coadsorption geometry of CO + O pair from CO_2 dissociation (CO_2→CO + O) reaction on the (001), (010), and (110) Ta_3N_5 surfaces. At the Ta_3N_5(001) surface, the oxygen atom binds at Ta site, whereas the carbon of the CO moiety bridges two N atoms, as shown in Figure 5a, releasing a coadsorption energy of −1.64 eV. At the Ta_3N_5(010) surface, the oxygen atom binds at bridge Ta sites, whereas the carbon of the CO moiety binds at the N site, as shown in Figure 5b, releasing a coadsorption energy of −2.99 eV. At the Ta_3N_5(110) surface, as shown in Figure 5c, the oxygen atom and the carbon of the CO moiety bind at Ta and N sites, respectively, releasing a coadsorption energy of −0.68 eV. The results show that the coadsorption of (CO + O) pairs is more favourable on the Ta_3N_5(010), followed by Ta_3N_5(001), and then the Ta_3N_5(110) surface. The geometrical parameters and calculated coadsorption (E_{coads}), reaction (E_{rxn}), and the activation energy barriers (E_{act}) of CO_2 dissociation are shown in Table 2. The Ta_3N_5(010) surface exhibits the lowest CO_2/Ta_3N_5(010)→(CO + O)/Ta_3N_5(010) reaction energy—exothermic by −1.09 eV. The CO_2→CO + O reaction is, however, endothermic by 1.04 and 0.52 eV on the Ta_3N_5(001) and Ta_3N_5(110) surfaces, respectively. The activation energy barrier (E_{act}) for the dissociation of CO_2 on the (001), (010), and (110) Ta_3N_5 surfaces are calculated at 1.34, 1.15 and 1.56 eV, respectively. The higher E_{act} and the endothermic E_{rxn} for the dissociation of CO_2 predicted on the (001) and (110) surfaces suggest that direct dissociation may be hindered at room temperature and without surface promoters such as H_2O and H species. Direct CO_2 dissociation may, however, occur at room temperature on the Ta_3N_5(010) surface owing to its calculated exothermic E_{rxn} and the lower E_{act}.

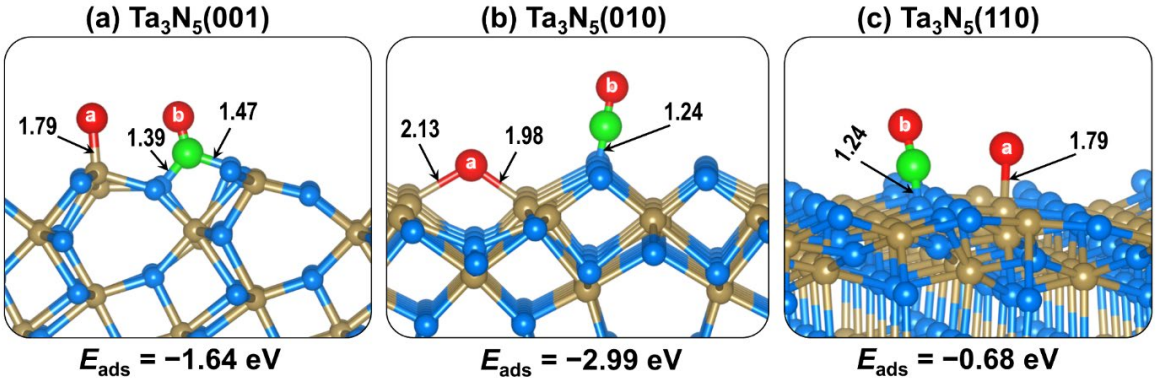

Figure 5. Lowest-energy coadsorption structures of CO + O pairs on (**a**) (001), (**b**) (010), and (**c**) (110) Ta_3N_5 surfaces.

Table 2. Coadsorption (E_{coads}), reaction (E_{rxn}), activation (E_{act}) energies and geometrical parameters of (CO + O) pairs on Ta_3N_5(001), (010), and (110) surfaces.

Parameter	Ta_3N_5(001)	Ta_3N_5(010)	Ta_3N_5(110)
E_{coads} (eV)	−1.69	−2.99	−0.68
E_{rxn} (eV)	1.04	−1.09	0.52
E_{act} (eV)	1.34	1.15	1.56
d(C−N) (Å)	1.467/1.388	1.237	1.242
d(O_a−Ta) (Å)	1.788	2.126/1.979	1.788
d(C−O_b) (Å)	1.227	1.173	1.170

2.4. CO_2 and H_2O Coadsorption and Reactions

Water is a suitable source of hydrogen for CO_2 conversion via its hydrogenation to valued-added chemicals [54]. As such, investigations of H_2O and CO_2 coadsorption and the possible reactions between them are indisputable. Prior to investigating the coadsorption structures of CO_2 and H_2O, the most stable adsorption geometries of isolated H_2O on the (001), (010), and (110) Ta_3N_5 surfaces were systematically characterized. The calculated energetics and structural parameters for molecular and dissociative water adsorption on the three Ta_3N_5 surfaces are presented in Table 3 and Figure 6. The most stable adsorption of water is predicted at the Ta sites via its O atoms. The adsorption energy of molecular water at the (001), (010), and (110) Ta_3N_5 surfaces is calculated to be −1.42, −1.07, and −1.08 eV, respectively, indicating that the interaction is strongest at the (001) surface and weakest on the (110) surface, similar to the trend predicted for CO_2 adsorption. The most stable dissociative water adsorption configurations (OH + H pair) provided in the rightmost panel of Figure 6 show that when dissociated, the OH species preferentially bind to the Ta sites through the O atom, whereas the H atoms bind at the N sites. From Table 3, it is worth noting that the dissociative adsorption of water on three surfaces is thermodynamically more favourable than molecular adsorption as reflected is the larger coadsorption energies released by the OH + H pairs. The H_2O→OH + O reaction energies on the (001), (010), and (110) surfaces can be calculated at −1.15, −0.28, and −1.03 eV, respectively, all of which are exothermic and thus indicate favourable dissociation of water. The interacting Ta−OH distances are calculated at 1.987, 2.297, and 1.978 Å, whereas the N−H distances were converged at 1.031, 1.056, and 1.022 Å on the (001), (010), and (110) surfaces, respectively. The transition states structures were determined (central panels, Figure 6) in order to estimate the activation energy barriers for the dissociation of water, which were predicted at 0.18, 0.34, and 0.27 eV at the (001), (010), and (110) surfaces, respectively. In a previous study the energy barriers for the dissociation of water was calculated at to be as low as 0.05 eV on the Ta_3N_5(110) surface [55]. Compared to direct CO_2 dissociation, the predicted low activation energy barriers and the exothermic reaction energies suggest that spontaneous water dissociation will occur on the (001), (010), and (110) surfaces.

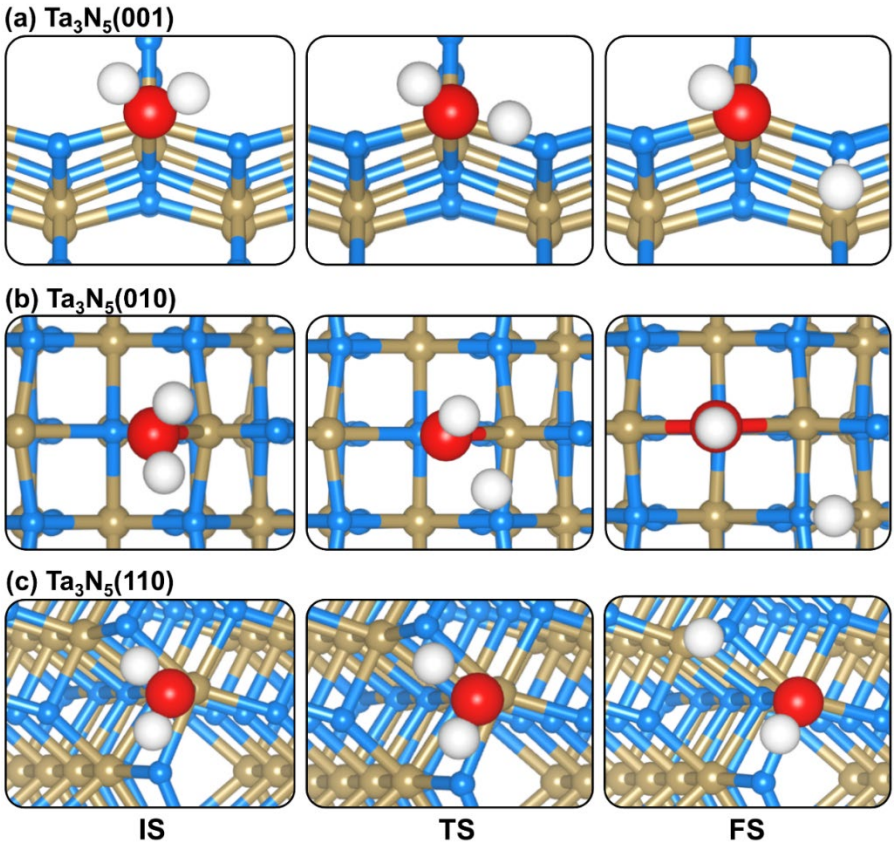

Figure 6. Optimized structures for the initial (left panels), transition (middle panels), and final (right panels) states of the most favourable path for the $H_2O \rightarrow OH + H$ reaction on (**a**) (001), (**b**) (010), and (**c**) (110) Ta_3N_5 surfaces. (Atomic colour scheme: Ta = pale olive, N = blue, O = red, and H = white.)

Table 3. Coadsorption (E_{coads}), reaction (E_{rxn}), activation (E_{act}) energies and geometrical parameters of (OH + H) pairs on Ta_3N_5(001), (010), and (110) surfaces.

Parameter	Ta_3N_5(001)		Ta_3N_5(010)		Ta_3N_5(110)	
State	Molecular	Dissociative	Molecular	Dissociative	Molecular	Dissociative
E_{ads} (eV)	−1.42	−2.16	−1.07	−1.35	−1.08	−2.12
E_{rxn} (eV)	-	−0.74	-	−0.28	-	−1.04
E_{act} (eV)	0.18	-	0.34	-	0.27	-
d(O−Ta) (Å)	2.307	1.987	2.395	2.297	2.295	1.978
d(H−N) (Å)	-	1.031	-	1.056	-	1.022
d(O−H) (Å)	0.977/0.977	0.969	0.980/0.979	0.976	0.986/1.006	0.970

The lowest-energy coadsorption structures of $CO_2 + H_2O$ on the (001), (010), and (110) surfaces of have been characterized, as shown in Figure 7. The coadsorption energy of $CO_2 + H_2O$ on the different surfaces is calculated as follows:

$$E_{coads} = E_{(CO_2+H_2O)/surface} - (E_{surface} + E_{CO_2} + E_{H_2O}) \quad (2)$$

where $E_{(CO_2+H_2O)/surface}$, E_{CO_2}, E_{H_2O} and $E_{surface}$ are the total energy of the coadsorbed (CO_2+H_2O) surface system, the free CO_2, the free H_2O, and the bare Ta_3N_5 surfaces, respectively. The calculated CO_2 + H_2O coadsorption energies and the geometrical parameters are presented in Table 4. The coadsorption energy for the CO_2 + H_2O pair on the (001), (010), and (110) Ta_3N_5 surfaces were calculated at −3.94, −3.68, and −2.43 eV, respectively. Consistent with attractive interactions, the coadsorption energies are more exothermic than the sum of the separate CO_2 and H_2O adsorption energies.

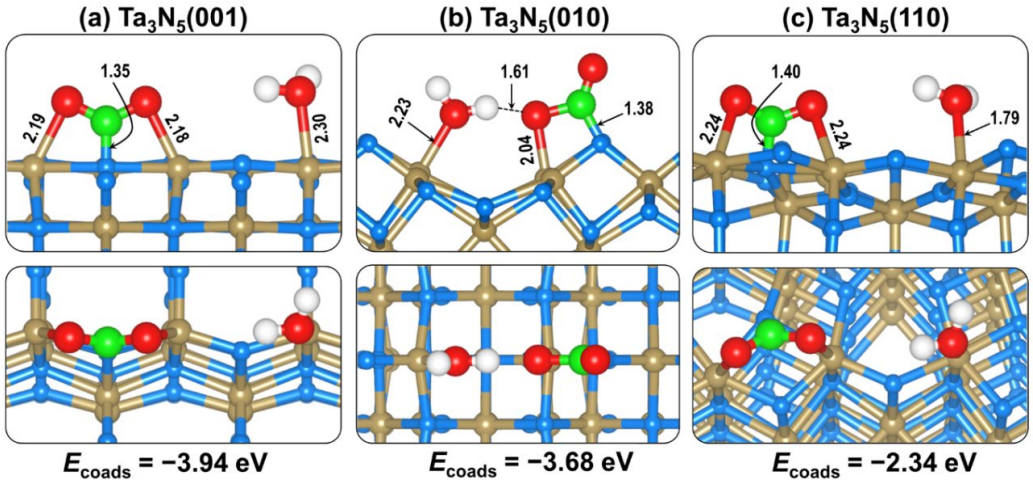

Figure 7. Lowest energy of coadsorption structures of CO_2 + H_2O on (**a**) (001), (**b**) (010), and (**c**) (110) Ta_3N_5 surfaces. (Atomic colour scheme: Ta = pale olive, N = blue, C = green, O = red, and H = white.)

Table 4. Coadsorption energies and structural parameters for CO_2 + H_2O on Ta_3N_5(001), (010), and (110) surfaces.

Parameter	Ta_3N_5(001)	Ta_3N_5(010)	Ta_3N_5(110)
E_{coads} (eV)	−3.94	−3.68	−2.34
$\Delta q(CO_2+H_2O)$ (|e|)	0.40	0.35	0.31
$\Delta q(H_2O)$ (|e|)	0.03	0.03	0.02
d(C−O_a) (Å)	1.305	1.460	1.292
d(C−O_b) (Å)	1.307	1.202	1.292
$\angle O_aCO_b$ (°)	125.6	122.1	125.5
d(C−N) (Å)	1.354	1.378	1.399
d(O_a−Ta) (Å)	2.187	2.045	2.231
d(O_b−Ta) (Å)	2.188	-	2.244
d(O_w−H) (Å)	0.981	1.022	0.978
d(O_w−Ta) (Å)	2.299	2.226	2.315
d(O–H) (Å)	3.619	1.606	3.454

Analysis of the differential charge density isosurface contours (Figure 8) shows accumulation of electron density within the C–N and O–Ta bonding regions, indicating chemisorption.

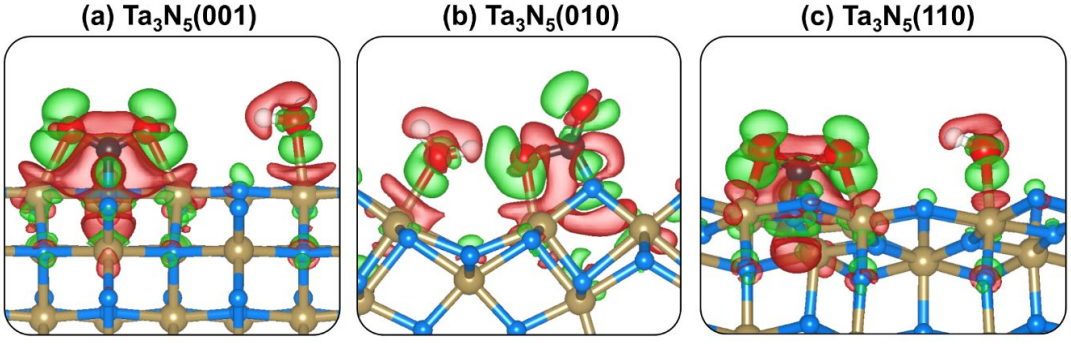

Figure 8. Differential charge density isosurface contours of the CO_2 + H_2O coadsorption on Ta_3N_5 (**a**) (001), (**b**) (010), and (**c**) (110) surfaces. The green contours denote electron density increase whereas the red contours denote electron density decrease by 0.02 e/Å^3, respectively. (Atomic colour scheme: Ta = pale olive, N = blue, C = green, and O = red.)

Hydrogen-bonded interactions between the CO_2 and H_2O species are observed at the $Ta_3N_5(010)$ surface, evident by the close interaction of the electron density of the two species. This may favour proton transfer to the CO_2 molecule, which has been investigated and found to results in spontaneous dissociation of the surface-bound C−O bond to form CO and $2OH^-$ species (Figure 9a). Relative to the initial coadsorbed CO_2 + H_2O system, the reaction energy for the formation of the CO + $2OH^-$ species on the $Ta_3N_5(010)$ surface is calculated to be highly exothermic by 1.11 eV. When the proton is transferred to the unbound O of CO_2, a stable carboxyl COOH species (Figure 9b) is formed with a reaction energy of −0.67 eV. No stable formate HCOO species is formed as the attached proton to the C atom detaches during energy minimisation to the surface N site, as shown in Figure 9c, with the reaction energy calculated to be −0.19 eV. These results suggest that the $Ta_3N_5(010)$ surface favours the dissociation CO_2 in the presence of H_2O, and the resulting CO species could be further hydrogenated to form CH_2O and CH_3OH.

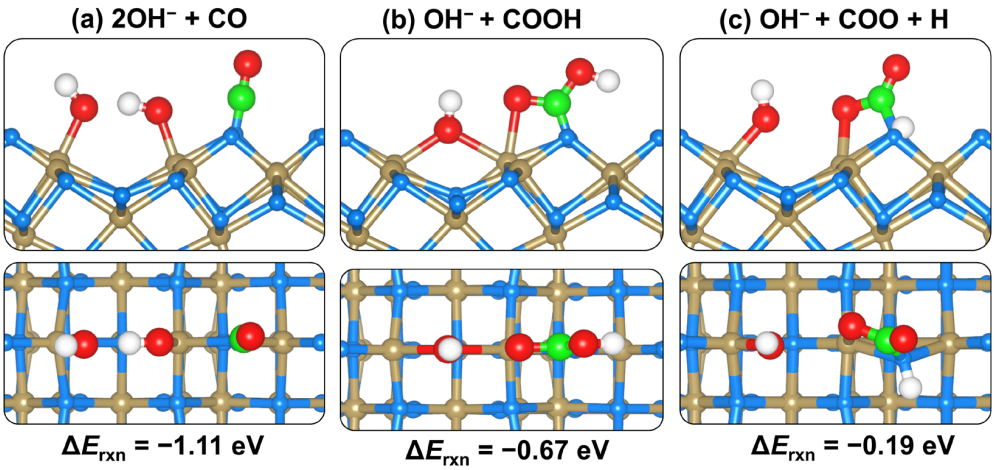

Figure 9. Optimized structures of the reaction products of proton transfer from H_2O to CO_2 on $Ta_3N_5(010)$ surface. (**a**) Proton transfer to surface-bound O atom, (**b**) proton transfer to unbound O atom and (**c**) proton transfer to the C atom. (Atomic colour scheme: Ta = pale olive, N = blue, C = green, and O = red.)

Compared to the $Ta_3N_5(010)$ surface, the reaction energy for the proton transfer from H_2O to CO_2 to form COOH and HCOO species is found to be highly endothermic on the $Ta_3N_5(001)$ and $Ta_3N_5(110)$ surfaces, as shown in Figure 10. The less endothermic reaction energies predicted for the COOH species than for the HCOO species, however, suggest that further hydrogenation reactions to products will proceed via the carboxyl COOH route.

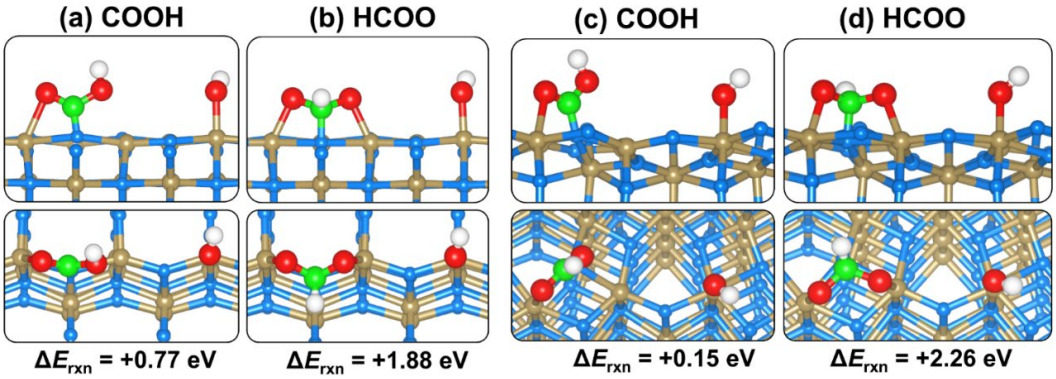

Figure 10. Optimized structures of the reaction products of proton transfer from H_2O to CO_2 to COOH and HCOO species on (**a**,**b**) $Ta_3N_5(001)$ and (**c**,**d**) $Ta_3N_5(110)$ surfaces. (Atomic colour scheme: Ta = pale olive, N = blue, C = green, and O = red.)

3. Summary and Conclusions

This work presents comprehensive first-principles density functional theory analyses of the adsorption and activation of CO_2 in the absence and presence of H_2O on the (001), (010), and (110) surfaces of Ta_3N_5, a photocatalyst able to absorb visible light to initiate photocatalysis. The strength of adsorption and extent of CO_2 activation is found to be influenced by the stability of the different Ta_3N surfaces, where it adsorbs most strongly onto the least stable Ta_3N_5(001) surface and most weakly onto the most stable Ta_3N_5(110) surface. Direct dissociation of CO_2 is suggested to occur on the Ta_3N_5(010) surface owing to the calculated exothermic reaction energy and lower activation energy barrier. In contrast, direct CO_2 dissociation would be hindered on the Ta_3N_5(001) and Ta_3N_5(110) surfaces without surface promoters such as H_2O and H species. Spontaneous water dissociation is predicted occur on the (001), (010), and (110) surfaces, providing the necessary hydrogen source for CO_2 reduction reactions. The strongest attractive interaction between coadsorbed CO_2 and H_2O is predicted on the Ta_3N_5(010) surface, which gave rise to proton transfer to the CO_2 molecule, causing its spontaneous dissociation to form CO and $2OH^-$ species with an exothermic reaction energy of −1.11 eV. The formation of COOH* and HCOO* intermediates is found to be highly endothermic on the Ta_3N_5(001) and Ta_3N_5(110) surfaces, although the COOH* species are less endothermic, indicating that further hydrogenation reactions will proceed via the carboxyl COOH* route. A further hydrogenation of the OH end of the COOH* intermediate may lead to CO + H_2O formation, where the formed CO species could be further hydrogenated towards methane of methanol formation. This is consistent with the findings of Lu et al. [37], who, based on their detected intermediates, suggested that the possible reaction pathway for CO_2 reduction over the Ta_3N_5 catalysts is CO_2→COOH*→CO→CH^*_x→CH_4. The present results demonstrate that Ta_3N_5 can efficiently activate the CO_2 molecule and photocatalytically reduce it with water to produce value-added fuels. Future investigations of the Eley–Rideal type of mechanism will be important to draw a direct comparison with the Langmuir–Hinshelwood mechanism unravelled in the present study. Further investigations of the effects of transition metal doping on the electronic structure and CO_2 conversion reactions over Ta_3N_5 catalyst under visible light will also be important.

4. Computational Details

The density functional theory (DFT) calculations were performed within the VASP package [55–58]. The projected augmented wave (PAW) method [59] was employed to describe the interactions between the valence electrons and the ionic core. Geometry optimisations were carried out using the Perdew−Burke−Enzerhof (PBE) generalized gradient approximation (GGA) functional [60], while the Hubbard U correction (PBE+U) was employed for accurate determination of the electronic structures [61–64]. From an analysis of how the electronic band gap increases with increasing strength of the on-site Coulomb repulsion, it was found that an effective *U* of 6.5 eV gives an accurate description of the structural parameters and the electronic properties of Ta_3N_5 [65]. Dispersion forces were accounted for through the Grimme DFT-D3 scheme [66]. The kinetic energy cut off was set to 600 eV, which ensured convergence of the total energy of the Ta_3N_5 to within 10^{-6} eV and the residual Hellman−Feynman forces to within 10^{-3} eV $Å^{-1}$. A 7 × 3 × 3 mesh of Monkhorst−Pack [67] k-points was used to sample the Brillouin zone of Ta_3N_5. For accurate determination of the electronic structure of Ta_3N_5, a higher mesh of 9 × 5 × 5 was used.

The (001), (010), and (110) surfaces, which are commonly observed in Ta_3N_5 nanoparticles, were created from the optimized bulk material using the METADISE code [68,69], which ensures the creation of surfaces with zero dipole moment perpendicular to the surface plane. In each simulation cell (slab thickness of at least 15 Å), a vacuum region of 20 Å was added in the z direction to avoid interactions between periodic slabs. The relative stabilities of the (001), (010), and (110) Ta_3N_5 surfaces were determined according to their relaxed surface energy (γ_r), calculated as:

$$\gamma_r = \frac{E_{slab}^{relaxed} - nE_{bulk}}{2A} \quad (3)$$

where $E_{slab}^{relaxed}$ is the energy of the relaxed slab, nE_{bulk} is the energy of an equal number (n) of the bulk Ta_3N_5 atoms, and A is the area of the slab surface. The adsorption energy (E_{ads}) of CO_2 and H_2O species is determined as follows:

$$E_{ads}\ (M) = E_{M+surface} - (E_{surface} + E_M) \quad (4)$$

where $E_{M+surface}$ is the total energy of the relaxed M+Ta_3N_5 systems (M = CO_2 and H_2O), $E_{surface}$ the total energy of the naked Ta_3N_5 surfaces alone, and E_M the total energy of the isolated adsorbates (CO_2 and H_2O). Because of the adsorption of reactant molecules at only one side of the surface, Makov–Payne dipole correction was applied perpendicular to each surface [70]. In order to determine the preferred adsorption sites and lowest energy adsorption modes of CO_2 and H_2O molecules on the Ta_3N_5 surfaces, different initial orientations of the molecules were optimized without any symmetry constraints. Charge transfer between the surfaces and adsorbates is quantified via Bader charge analysis [71]. Transition states (TS) along reaction pathways were determined using the climbing-image nudged elastic band (CI-NEB) method [72], wherein six images were generated between the states of reactants (IS) and products (FS) in each elementary process. Located TS were characterized by only one imaginary frequency, corresponding to the reaction coordinate. The reaction activation energy barrier (E_A) is determined by E_A = TS – IS, whereas the reaction energy (E_R) is determined by E_R = FS – IS.

Supplementary Materials: The following are available online at http://www.mdpi.com/2073-4344/10/10/1217/s1, Figure S1: Contains the relaxed structures of all possible adsorption CO_2 geometries on Ta_3N_5 (001), (010), and (110) surfaces.

Funding: This research was funded by the UK's Engineering and Physical Sciences Research Council (EPSRC), grant number EP/S001395/1.

Acknowledgments: The simulations were performed using the computational facilities of the Advanced Research Computing @ Cardiff (ARCCA) Division, Cardiff University. This work also made use of the facilities of ARCHER (http://www.archer.ac.uk), the UK's national supercomputing service, via our membership of the UK's HEC Materials Chemistry Consortium, which is funded by EPSRC (EP/L000202). Information on the data that underpins the results presented here, including how to access them, can be found in the Cardiff University data catalogue at http://doi.org/10.17035/d.2020.0119220581

Conflicts of Interest: The author declares no conflict of interest.

References

1. Li, K.; Peng, B.; Peng, T. Recent Advances in Heterogeneous Photocatalytic CO_2 Conversion to Solar Fuels. *ACS Catal.* **2016**, *6*, 7485–7527. [CrossRef]
2. Chang, X.; Wang, T.; Gong, J. CO_2 photo-reduction: Insights into CO_2 activation and reaction on surfaces of photocatalysts. *Energy Environ. Sci.* **2016**, *9*, 2177–2196. [CrossRef]
3. Habisreutinger, S.N.; Schmidt-Mende, L.; Stolarczyk, J.K. Photocatalytic Reduction of CO_2 on TiO_2 and Other Semiconductors. *Angew. Chem. Int. Ed.* **2013**, *52*, 7372–7408. [CrossRef] [PubMed]
4. Lingampalli, S.R.; Ayyub, M.M.; Rao, C.N.R. Recent Progress in the Photocatalytic Reduction of Carbon Dioxide. *ACS Omega* **2017**, *2*, 2740–2748. [CrossRef]
5. Inoue, T.; Fujishima, A.; Konishi, S.; Honda, K. Photoelectrocatalytic Reduction of Carbon Dioxide in Aqueous Suspensions of Semiconductor Powders. *Nature* **1979**, *277*, 637–638. [CrossRef]
6. Morris, A.J.; Meyer, G.J.; Fujita, E. Molecular Approaches to the Photocatalytic Reduction of Carbon Dioxide for Solar Fuels. *Acc. Chem. Res.* **2009**, *42*, 983–1994. [CrossRef]
7. Varghese, O.K.; Paulose, M.; LaTempa, T.J.; Grimes, C.A. High-Rate Solar Photocatalytic Conversion of CO_2 and Water Vapor to Hydrocarbon Fuels. *Nano Lett.* **2009**, *9*, 731–737. [CrossRef]
8. Roy, S.C.; Varghese, O.K.; Paulose, M.; Grimes, C.A. Toward Solar Fuels: Photocatalytic Conversion of Carbon Dioxide to Hydrocarbons. *ACS Nano* **2010**, *4*, 1259–1278. [CrossRef]
9. Li, Y.; Chan, S.H.; Sun, Q. Heterogeneous Catalytic Conversion of CO_2: A Comprehensive Theoretical Review. *Nanoscale* **2015**, *7*, 8663–8683. [CrossRef]

10. Todorova, T.K.; Schreiber, M.W.; Fontecave, M. Mechanistic Understanding of CO_2 Reduction Reaction (CO2RR) Toward Multicarbon Products by Heterogeneous Copper-Based Catalysts. *ACS Catal.* **2020**, *10*, 1754–1768. [CrossRef]
11. Paulino, P.N.; Salim, V.M.M.; Resende, N.S. Zn-Cu promoted TiO_2 photocatalyst for CO_2 reduction with H_2O under UV light. *Appl. Catal. B Environ.* **2016**, *185*, 362–370. [CrossRef]
12. Liu, L.; Zhao, H.; Andino, J.M.; Li, Y. Photocatalytic CO_2 Reduction with H_2O on TiO_2 Nanocrystals: Comparison of Anatase, Rutile, and Brookite Polymorphs and Exploration of Surface Chemistry. *ACS Catal.* **2012**, *2*, 1817–1828. [CrossRef]
13. Mino, L.; Spoto, G.; Ferrari, A.M. CO_2 Capture by TiO_2 Anatase Surfaces: A Combined DFT and FTIR Study. *J. Phys. Chem. C* **2014**, *118*, 25016–25026. [CrossRef]
14. Ye, J.Y.; Liu, C.-J.; Ge, Q.F. DFT Study of CO_2 Adsorption and Hydrogenation on the In_2O_3 Surface. *J. Phys. Chem. C* **2012**, *116*, 7817–7825. [CrossRef]
15. Ye, J.Y.; Liu, C.-J.; Mei, D.H.; Ge, Q.F. Active Oxygen Vacancy Site for Methanol Synthesis from CO_2 Hydrogenation on In_2O_3(110): A DFT Study. *ACS Catal.* **2013**, *3*, 1296–1306. [CrossRef]
16. Pa, Y.X.; Mei, D.; Liu, C.J.; Ge, Q. Adsorption on Ga_2O_3 Surface: A Combined Experimental and Computational Study. *J. Phys. Chem. C* **2011**, *115*, 10140–10146.
17. Pan, Y.X.; Liu, C.-J.; Mei, D.H.; Ge, Q.F. Effects of Hydration and Oxygen Vacancy on CO_2 Adsorption and Activation on β-Ga_2O_3(100). *Langmuir* **2010**, *26*, 5551–5558. [CrossRef]
18. Pan, Y.X.; Liu, C.-J.; Ge, Q.F. Adsorption and Protonation of CO_2 on Partially Hydroxylated γ-Al_2O_3 Surfaces: A Density Functional Theory Study. *Langmuir* **2008**, *24*, 12410–12419. [CrossRef]
19. Pan, Y.X.; Liu, C.-J.; Ge, Q.F. Effect of surface hydroxyls on selective CO_2 hydrogenation over Ni4/γ-Al_2O_3: A density functional theory study. *J. Catal.* **2010**, *272*, 227–234. [CrossRef]
20. Liu, X.; Ye, L.; Liu, S.; Li, Y.; Ji, X. Photocatalytic Reduction of CO_2 by ZnO Micro/nanomaterials with Different Morphologies and Ratios of {0001} Facets. *Sci. Rep.* **2016**, *6*, 38474. [CrossRef]
21. Tang, Q.-L.; Luo, Q.-H. Adsorption of CO_2 at ZnO: A Surface Structure Effect from DFT+U Calculations. *J. Phys. Chem. C* **2013**, *117*, 22954–22966. [CrossRef]
22. Cheng, Z.; Sherman, B.J.; Lo, C.S. Carbon dioxide activation and dissociation on ceria (110): A density functional theory study. *J. Chem. Phys.* **2013**, *138*, 014702. [CrossRef] [PubMed]
23. Kumari, N.; Haider, M.A.; Agarwal, M.; Sinha, N.; Basu, S. Role of Reduced CeO_2(110) Surface for CO_2 Reduction to CO and Methanol. *J. Phys. Chem. C* **2016**, *120*, 16626–16635. [CrossRef]
24. Liu, Q.; Zhou, Y.; Kou, J.; Chen, X.; Tian, Z.; Gao, J.; Yan, S.; Zou, Z. High-Yield Synthesis of Ultralong and Ultrathin Zn2GeO4 Nanoribbons Toward Improved Photocatalytic Reduction of CO_2 into Renewable Hydrocarbon Fuel. *J. Am. Chem. Soc.* **2010**, *132*, 14385–14387. [CrossRef] [PubMed]
25. Mao, J.; Peng, T.; Zhang, X.; Li, K.; Zan, L. Selective methanol production from photocatalytic reduction of CO_2 on $BiVO_4$ under visible light irradiation. *Catal. Commun.* **2012**, *28*, 38–41. [CrossRef]
26. Sommers, J.M.; Alderman, N.P.; Viasus, C.J.; Gambarotta, S. Revisiting the behaviour of $BiVO_4$ as a carbon dioxide reduction photo-catalyst. *Dalton Trans.* **2017**, *46*, 6404–6408. [CrossRef] [PubMed]
27. Harb, M.; Cavallo, L.; Basset, J.-M. Designing an active Ta_3N_5 photocatalyst for H_2 and O_2 evolution reactions by specific exposed facet engineering: A first-principles study. *Phys. Chem. Chem. Phys.* **2020**, *22*, 10295–10304. [CrossRef]
28. Li, Y.; Takata, T.; Cha, D.; Takanabe, K.; Minegishi, T.; Kubota, J.; Domen, K. Vertically aligned Ta_3N_5 nanorod arrays for solar-driven photoelectrochemical water splitting. *Adv. Mater.* **2012**, *25*, 125–131. [CrossRef]
29. Kim, J.Y.; Lee, M.H.; Kim, J.-H.; Kim, C.W.; Youn, D.H. Facile nanocrystalline Ta_3N_5 synthesis for photocatalytic dye degradation under visible light. *Chem. Phys. Lett.* **2020**, *738*, 136900. [CrossRef]
30. Zhang, P.; Zhang, J.; Gong, J. Tantalum-based semiconductors for solar water splitting. *Chem. Soc. Rev.* **2014**, *43*, 4395–4422. [CrossRef]
31. He, Y.; Ma, P.; Zhu, S.; Liu, M.; Dong, Q.; Espano, J.; Yao, X.; Wang, D. Photo-Induced Performance Enhancement of Tantalum Nitride for Solar Water Oxidation. *Joule* **2017**, *1*, 831–842. [CrossRef]
32. Zhang, Q.; Gao, L. Ta_3N_5 nanoparticles with enhanced photocatalytic efficiency under visible light irradiation. *Langmuir* **2004**, *20*, 9821–9827. [CrossRef] [PubMed]
33. Ma, S.S.K.; Hisatomi, T.; Maeda, K.; Moriya, Y.; Domen, K. Enhanced water oxidation on Ta_3N_5 Photocatalysts by modification with alkaline metal salts. *J. Am. Chem. Soc.* **2012**, *134*, 19993–19996. [CrossRef] [PubMed]

34. Jones, D.R.; Gomez, V.; Bear, J.C.; Rome, B.; Mazzali, F.; McGettrick, J.; Lewis, A.R.; Margadonna, S.; Al-Masry, W.A.; Dunnill, C.W. Active removal of waste dye pollutants using $Ta_3N_5/W_{18}O_{49}$ nanocomposite fibres. *Sci. Rep.* **2017**, *7*, 4090. [CrossRef]
35. Jiang, Y.; Jing, X.; Zhu, K.; Peng, Z.Y.; Zhang, J.; Liu, Y.; Zhang, W.; Nia, L.; Liub, Z. Ta_3N_5 nanoparticles/TiO_2 hollow sphere (0D/3D) heterojunction: Facile synthesis and enhanced photocatalytic activities of levofloxacin degradation and H_2 evolution. *Dalton Trans.* **2018**, *47*, 13113–13125. [CrossRef]
36. Nguyen, T.D.C.; Nguyen, T.P.L.C.; Mai, H.T.T.; Dao, V.D.; Nguyen, M.P.; Nguyen, V.N. Novel photocatalytic conversion of CO_2 by vanadium-doped tantalum nitride for valuable solar fuel production. *J. Catal.* **2017**, *352*, 67–74. [CrossRef]
37. Lu, L.; Wang, S.; Zhou, C.; Shi, Z.; Zhu, H.; Xin, Z.; Wang, X.; Yan, S.; Zoua, Z. Surface chemistry imposes selective reduction of CO_2 to CO over Ta3N5/LaTiO2N photocatalyst. *J. Mater. Chem. A* **2018**, *6*, 14838–14846. [CrossRef]
38. Dzade, N.Y.; Roldan, A.; de Leeuw, N.H. Activation and dissociation of CO_2 on the (001), (011), and (111) surfaces of mackinawite (FeS): A dispersion-corrected DFT study. *J. Chem. Phys.* **2015**, *143*, 094703. [CrossRef]
39. Yin, W.J.; Krack, M.; Wen, B.; Ma, S.Y.; Liu, L.M. CO_2 Capture and Conversion on Rutile TiO_2(110) in the Water Environment: Insight by First-Principles Calculations. *J. Phys. Chem. Lett.* **2015**, *6*, 2538–2545. [CrossRef] [PubMed]
40. Santos-Carballal, D.; Roldan, A.; Dzade, N.Y.; de Leeuw, N.H. Reactivity of CO_2 on the surfaces of magnetite (Fe_3O_4), greigite (Fe_3S_4) and mackinawite (FeS). *Philos. Trans. R. Soc. A Math. Phys. Eng. Sci.* **2018**, *376*, 20170065.
41. Meng, X.G.; Ouyang, S.X.; Kako, T.; Li, P.; Yu, Q.; Wang, T.; Ye, J.H. Photocatalytic CO_2 conversion over alkali modified TiO_2 without loading noble metal cocatalyst. *Chem. Commun.* **2014**, *50*, 11517–11519. [CrossRef] [PubMed]
42. Toda, Y.; Hirayama, H.; Kuganathan, N.; Torrisi, A.; Sushko, P.V.; Hosono, H. Activation and splitting of carbon dioxide on the surface of an inorganic electride material. *Nat. Commun.* **2013**, *4*, 2378. [CrossRef] [PubMed]
43. Brese, N.E.; O'Keeffe, M.; Rauch, P.; DiSalvo, F.J. Structure of Ta_3N_5 at 16 K by time-of-flight neutron diffraction. *Acta Crystallogr. Sect. C Cryst. Struct. Commun.* **1991**, *47*, 2291. [CrossRef]
44. Morbec, J.M.; Narkeviciute, I.; Jaramillo, T.F.; Galli, G. Optoelectronic properties of Ta_3N_5: A joint theoretical and experimental study. *Phys. Rev. B* **2014**, *90*, 155204. [CrossRef]
45. Wang, J.; Luo, W.; Feng, J.; Zhang, L.; Li, Z.; Zou, Z. Theoretical study of water adsorption and dissociation on Ta_3N_5(100) surfaces. *Phys. Chem. Chem. Phys.* **2013**, *15*, 16054–16064. [CrossRef]
46. Fan, G.; Fang, T.; Wang, X.; Zhu, Y.; Fu, H.; Feng, J.; Li, Z.; Zou, Z. Interfacial Effects on the Band Edges of Ta_3N_5 Photoanodes in an Aqueous Environment: A Theoretical View. *iScience* **2019**, *13*, 432–439. [CrossRef]
47. Zeinalipour-Yazdi, C.D.; Hargreaves, J.S.J.; Laassiri, S.; Catlow, C.R.A. DFT-D3 study of H_2 and N_2 chemisorption over cobalt promoted Ta_3N_5-(100), (010) and (001) surfaces. *Phys. Chem. Chem. Phys.* **2017**, *19*, 11968–11974. [CrossRef]
48. Chun, W.-J.; Ishikawa, A.; Fujisawa, H.; Takata, T.; Kondo, J.N.; Hara, M.; Kawai, M.; Matsumoto, Y.; Domen, K. Conduction and Valence Band Positions of Ta_2O_5, TaON, and Ta3N5 by UPS and Electrochemical Methods. *J. Phys. Chem. B* **2003**, *107*, 1798–1803. [CrossRef]
49. Pinaud, B.A.; Vailionis, A.; Jaramillo, T.F. Controlling the Structural and Optical Properties of Ta_3N_5 Films through Nitridation Temperature and the Nature of the Ta Metal. *Chem. Mater.* **2014**, *26*, 1576–1582. [CrossRef]
50. Wang, J.; Feng, J.; Zhang, L.; Li, Z.; Zou, Z. Role of oxygen impurity on the mechanical stability and atomic cohesion of Ta3N5 semiconductor photocatalyst. *Phys. Chem. Chem. Phys.* **2014**, *16*, 15375–15380. [CrossRef]
51. Harb, M.; Basset, J.-M. Insights into the Most Suitable TiO_2 Surfaces for Photocatalytic O_2 and H_2 Evolution Reactions from DFT Calculations. *J. Phys. Chem. C* **2020**, *124*, 2472–2480. [CrossRef]
52. Suzuki, S.; Wagata, H.; Komatsus, M.; Minegishi, T.; Domen, K.; Oishia, S.; Teshima, K. A novel flux coating method for the fabrication of layers of visible-light-responsive Ta_3N_5 crystals on tantalum substrates. *Mater. Chem. A* **2015**, *3*, 13946–13952. [CrossRef]
53. Freund, H.-J.; Roberts, M.W. Surface chemistry of carbon dioxide. *Surf. Sci. Rep.* **1996**, *25*, 225–273. [CrossRef]
54. Kondratenko, E.V.; Mul, G.; Baltrusaitis, J.; Larrazáabal, G.O.; Pérez-Ramírez, J. Status and perspectives of CO_2 conversion into fuels and chemicals by catalytic, photocatalytic and electrocatalytic processes. *Energy Environ. Sci.* **2013**, *6*, 3112–3135. [CrossRef]

55. Wang, J.; Ma, A.; Li, Z.; Jiang, J.; Feng, J.; Zou, Z. Theoretical study on the surface stabilities, electronic structures and water adsorption behavior of the Ta_3N_5(110) surface. *Phys. Chem. Chem. Phys.* **2016**, *18*, 7938–7945. [CrossRef]
56. Kresse, G.; Hafner, J. Ab initio molecular dynamics for liquid metals. *Phys. Rev. B Condens. Matter Mater. Phys.* **1993**, *47*, 558–561. [CrossRef]
57. Kresse, G.; Joubert, D. From ultrasoft pseudopotentials to the projector augmented-wave method. *Phys. Rev. B Condens. Matter Mater. Phys.* **1999**, *59*, 1758. [CrossRef]
58. Kresse, G.; Furthmüller, J. Efficient iterative schemes for ab initio total-energy calculations using a plane-wave basis set. *Phys. Rev. B Condens. Matter Mater. Phys.* **1996**, *54*, 11169. [CrossRef]
59. Kresse, G.; Furthmüller, J. Efficiency of Ab-Initio Total Energy Calculations for Metals and Semiconductors Using a Plane-Wave Basis Set. *Comput. Mater. Sci.* **1996**, *6*, 15–50. [CrossRef]
60. Blöchl, P.E. Projector augmented-wave method. *Phys. Rev. B Condens. Matter Mater. Phys.* **1994**, *50*, 17953. [CrossRef]
61. Perdew, J.P.; Burke, K.; Ernzerhof, M. Generalized Gradient Approximation Made Simple. *Phys. Rev. Lett.* **1997**, *78*, 1396. [CrossRef]
62. Dzade, N.Y.; de Leeuw, N.H. Periodic DFT+U investigation of the bulk and surface properties of marcasite (FeS_2). *Phys. Chem. Chem. Phys.* **2017**, *19*, 27478–27488. [CrossRef] [PubMed]
63. Himmetoglu, B.; Floris, A.; de Gironcoli, S.; Cococcioni, M. Hubbard-corrected DFT energy functionals: The LDA+U description of correlated systems. *Int. J. Quantum Chem.* **2014**, *114*, 14–49. [CrossRef]
64. Anisimov, V.I.; Aryasetiawan, F.; Lichtenstein, A.I. First-principles calculations of the electronic structure and spectra of strongly correlated systems: The LDA+ U method. *J. Phys. Condens. Matter* **1997**, *9*, 767–808. [CrossRef]
65. Wang, J.; Fang, T.; Zhang, L.; Feng, J.; Li, Z.; Zou, Z. Effects of oxygen doping on optical band gap and band edge positions of Ta_3N_5 photocatalyst: A GGA plus U calculation. *J. Catal.* **2014**, *309*, 291–299. [CrossRef]
66. Grimme, S.; Antony, J.; Ehrlich, S.; Krieg, H. A consistent and accurate ab initio parametrization of density functional dispersion correction (DFT-D) for the 94 elements H-Pu. *J. Chem. Phys.* **2010**, *132*, 154104. [CrossRef] [PubMed]
67. Monkhorst, H.J.; Pack, J.D. Special points for Brillouin-zone integrations. *Phys. Rev. B Solid State* **1976**, *13*, 5188. [CrossRef]
68. Watson, G.W.; Kelsey, E.T.; de Leeuw, N.H.; Harris, D.J.; Parker, S.C. Atomistic simulation of dislocations, surfaces and interfaces in MgO. *J. Chem. Soc. Faraday Trans.* **1996**, *92*, 433. [CrossRef]
69. Tasker, P.W. The stability of ionic crystal surfaces. *J. Phys. C Solid State Phys.* **1979**, *12*, 4977. [CrossRef]
70. Makov, G.; Payne, M.C. Periodic boundary conditions in ab initio calculations. *Phys. Rev. B Condens. Matter Mater. Phys.* **1995**, *51*, 4014. [CrossRef]
71. Tang, W.; Sanville, E.; Henkelman, G. A grid-based Bader analysis algorithm without lattice bias. *J. Phys. Condens. Matter* **2009**, *21*, 84204. [CrossRef] [PubMed]
72. Mills, G.; Jónsson, H.; Schenter, G.K. Reversible work transition state theory: Application to dissociative adsorption of hydrogen. *Surf. Sci.* **1995**, *324*, 305–337. [CrossRef]